

Correlation of internal flow structure with heat transfer efficiency in turbulent Rayleigh-Bénard convection

Ao Xu,^{1, a)} Xin Chen,¹ Feng Wang,¹ and Heng-Dong Xi^{1, b)}

School of Aeronautics, Northwestern Polytechnical University, Xi'an 710072, China

(Dated: 16 September 2020)

To understand how internal flow structures manifest themselves in the global heat transfer, we study the correlation between different flow modes and the instantaneous Nusselt number (Nu) in a two-dimensional square Rayleigh-Bénard convection cell. High-resolution and long-time direct numerical simulations are carried out for Rayleigh number between 10^7 and 10^9 and Prandtl number of 5.3. The investigated Nusselt numbers include the volume-averaged Nu_{vol} , the wall-averaged Nu_{wall} , the kinetic energy dissipation based $Nu_{kinetic}$ and the thermal energy dissipation based $Nu_{thermal}$. The Fourier mode decomposition and proper orthogonal decomposition are adopted to extract the coherent flow structure. Our results show that the single-roll mode, the horizontally stacked double-roll mode, and the quadrupolar flow mode are more efficient for heat transfer on average. In contrast, the vertically stacked double roll mode is inefficient for heat transfer on average. The volume-averaged Nu_{vol} and the kinetic energy dissipation based $Nu_{kinetic}$ can better reproduce the correlation of internal flow structure with heat transfer efficiency than that of the wall-averaged Nu_{wall} and the thermal energy dissipation based $Nu_{thermal}$, even though these four Nusselt numbers give consistent time-averaged mean values. The ensemble-averaged time trace of Nu during flow reversal shows that only the volume-averaged Nu_{vol} can reproduce the overshoot phenomena that is observed in the previous experimental study. Our results reveal that the proper choice of the Nu is critical to obtain a meaningful interpretation. ^a

^{a)} The following article has been submitted to *Physics of Fluids*. After it is published, it will be found at Link (<https://publishing.aip.org/resources/librarians/products/journals/>).

^{a)}Electronic mail: axu@nwpu.edu.cn

^{b)}Electronic mail: hengdongxi@nwpu.edu.cn

I. INTRODUCTION

Thermal convection occurs ubiquitously in nature and has wide applications in industry. A paradigm for the study of thermal convection is the Rayleigh-Bénard (RB) convection, which is a fluid layer heated from the bottom and cooled from the top¹⁻⁶. The control parameters of the RB system include the Rayleigh number (Ra) and the Prandtl number (Pr). The Ra describes the strength of buoyancy force relative to thermal and viscous dissipative effects as $Ra = \beta g \Delta_T H^3 / (\nu \kappa)$. The Pr represents the thermophysical fluid properties as $Pr = \nu / \kappa$. Here, H is the fluid layer height, Δ_T is the imposed temperature difference. β , κ , and ν are the thermal expansion coefficient, thermal diffusivity and kinematic viscosity of the fluid, respectively. g is the gravitational acceleration. One of the response parameters of the RB system is the Nusselt number (Nu), which describes the global heat transfer efficiency of the system and is generally calculated as $Nu = J_{\text{total}} / J_{\text{conduction}}$. Here, J_{total} is the total heat flux and $J_{\text{conduction}}$ is the heat flux due to pure conduction across the bottom and top walls. In an RB experiment⁷⁻¹¹, the instantaneous Nu is calculated as $Nu(t) = (Q/S) / [\chi \Delta T(t)/H]$, where Q is the power supplied to the RB convection cell, S is the cross-sectional area of the cell, and χ is the thermal conductivity of the fluid. The temperature difference between the bottom and top walls is $\Delta T(t) = T_b(t) - T_t(t)$, where the temperatures of the bottom and top walls $T_b(t)$ and $T_t(t)$ are based on the average values of the two embedded thermistors in each plate.

In an RB direct numerical simulation (DNS), there are several different approaches to calculate the Nu . Before brief reviewing these approaches, we first introduce the following dimensionless variables:

$$\begin{aligned} \mathbf{x}/H &\rightarrow \mathbf{x}^*, \quad t/\sqrt{H/(\beta g \Delta_T)} \rightarrow t^*, \quad \mathbf{u}/\sqrt{\beta g H \Delta_T} \rightarrow \mathbf{u}^*, \\ p/(\rho_0 g \beta \Delta_T L_0) &\rightarrow p^*, \quad (T - T_0)/\Delta_T \rightarrow T^* \end{aligned} \quad (1)$$

Here, T_0 denotes the reference temperature. \mathbf{x} , t , \mathbf{u} , p and T are the position, time, velocity, pressure and temperature, respectively. Their counterparts with the asterisk superscript (*) denote the dimensionless variables. The first approach to calculate the Nu is based on volume-averaged velocity and temperature fields^{12,13} as $Nu_{\text{vol}} = \sqrt{Ra Pr} \langle w^* T^* \rangle_{V,t} + 1$, where w^* is the dimensionless vertical velocity component. Here, $\langle \cdots \rangle_{V,t}$ denotes the ensemble average over the whole convection cell and over the time. We assume the two parallel hot and cold walls are perpendicular to the vertical direction z . In this approach, the volume-averaged heat flux across the cell is $\langle wT - \kappa \partial T / \partial z \rangle_{V,t}$, and the heat flux due to pure conduction is

$\kappa\Delta T/H$, thus $Nu_{\text{vol}} = \langle wT - k\partial T/\partial z \rangle_{V,t} / (\kappa\Delta T/H) = \sqrt{RaPr} \langle w^*T^* \rangle_{V,t} - \langle \partial T^*/\partial z^* \rangle_{V,t}$; meanwhile, the top and the bottom walls remain constant cold and hot temperatures, respectively, we then have the term $\langle \partial T^*/\partial z^* \rangle_{V,t} = -1$. The second approach is to directly calculate the mean heat flux at the top and bottom walls^{12,13} as $Nu_{\text{wall}} = -(\langle \partial_z^* T^* \rangle_{\text{top},t} + \langle \partial_z^* T^* \rangle_{\text{bottom},t})/2$. Here, $\langle \cdots \rangle_{\text{top/bottom},t}$ denotes the ensemble average over the top (or bottom) wall and over the time. This approach takes advantage of the no-slip boundary conditions at the walls, thus $Nu_{\text{top/bottom}} = \langle -\kappa\partial T/\partial z \rangle_{\text{top/bottom},t} / (\kappa\Delta T/H) = -\langle \partial T^*/\partial z^* \rangle_{\text{top/bottom},t}$, and we then take the mean value of Nu_{top} and Nu_{bottom} as the Nu_{wall} . The third and fourth approaches are based on kinetic and thermal energy dissipation fields as $Nu_{\text{kinetic}} = 1 + \sqrt{RaPr} \langle \epsilon_u^* \rangle_{V,t}$ and $Nu_{\text{thermal}} = \sqrt{RaPr} \langle \epsilon_T^* \rangle_{V,t}$, respectively. Here, the kinetic and thermal energy dissipation rates in dimensional form are defined as $\epsilon_u(\mathbf{x},t) = (\nu/2) \sum_{ij} [\partial_i u_j(\mathbf{x},t) + \partial_j u_i(\mathbf{x},t)]^2$ and $\epsilon_T(\mathbf{x},t) = \kappa \sum_i [\partial_i T(\mathbf{x},t)]^2$, respectively. These two approaches utilize the exact relations of Nusselt numbers and global averages of the kinetic and thermal energy dissipation^{14,15} as $\langle \epsilon_u^* \rangle_{V,t} = (Nu - 1)/\sqrt{RaPr}$ and $\langle \epsilon_T^* \rangle_{V,t} = Nu/\sqrt{RaPr}$, respectively. These exact relations were obtained by averaging the equation of motion and heat equation, which further form the backbone of the Grossmann-Lohse (GL) theory on turbulent heat transfer^{16,17}. It should be noted that the above four approaches to calculate the Nusselt numbers would give consistent values if the DNS is well resolved and statistically convergent, but not *vice versa*. For example, Kooij et al.¹⁸ observed ripples in instantaneous snapshots of temperature field near sharp gradients when the simulation is under-resolved, while the above four Nusselt numbers from the simulation still look reasonable.

Previous studies have shown connections between the Nu and the flow structures in the RB system^{19–24}. Sun et al.¹⁹ experimentally measured the Nu in a cylindrical leveled cell (in which the large-scale circulation plane azimuthal sweeps) and in a tilted cell (in which the large-scale circulation, i.e., the LSC, is locked in a particular orientation). Results showed that the Nu is larger in the leveled cell than that in the tilted one, thus demonstrating different flow structures can give rise to different values of Nu . Xi and Xia²⁰ further observed both the single-roll structure and the double-roll structure in the large-scale flow. They examined the conditional average Nu (i.e., the average Nu corresponding to a particular flow structure) and found the single-roll flow structure is more efficient for heat transfer than the double-roll structure. Van der Poel et al.^{22,23} numerically simulated the aspect ratio dependence of the Nu in a two-dimensional (2D) square cell. They conditionally averaged the Nu based on flow structures and found that heat transfer is more efficient with less vertically arranged vortices or less horizontally elongated vortices. On the

other hand, an interesting feature of the LSC is the spontaneous and random directional reversal, which is related with reversal of the Earth's magnetic field²⁵ and reversals of the convective wind in the atmosphere²⁶. During flow reversal in the RB convection, the Nu first drops to its minima (corresponding to the breakup of the main roll), and then increases to its normal value (corresponding to the re-establishment of the main roll). Xi et al.²⁴ experimentally observed that the Nu has a momentary overshoot above its average value during flow reversal. The overshoot in Nu was attributed to more coherent flow or plumes for the short period of time during reversal. In short, a more coherent flow would produce a higher heat transfer efficiency, thus a larger Nu value.

An effective approach to extract internal flow structures from turbulence dataset is flow mode decomposition analysis, such as Fourier mode decomposition^{27,28} and proper orthogonal decomposition (POD) analysis^{29,30}. In these approaches, the instantaneous flow field is projected onto orthogonal basis, the instantaneous amplitude of the flow mode serves as the metrics to measure the strength of each flow mode. The relationship between heat transfer efficiency and each flow mode can be obtained by calculating their cross-correlation function. A positive correlation would suggest the flow mode produces more efficient heat transfer on average, and *vice versa*. In this work, we compare the features of four different Nusselt numbers (i.e., Nu_{vol} , Nu_{wall} , $Nu_{kinetic}$, $Nu_{thermal}$), particularly their abilities on revealing the connection between heat transfer efficiency and flow structures in the RB turbulent convection. As will become clear, proper choice of the Nu is critical to obtain a meaningful interpretation on how the flow structure affects global heat transfer. Meanwhile, we should note the advantages and disadvantages of each flow mode decomposition analysis approach. First, in Fourier mode decomposition, we have to pre-design an appropriate Fourier basis, which may be nontrivial for complex geometry of flow domain; in contrast, the POD does not require prior knowledge of the geometry of the flow domain. Secondly, the POD modes are ranked with respect to their energy content, while the same Fourier mode can be adopted for flows with different control parameters (e.g., Ra and Pr).

The rest of this paper is organized as follows: In Sec. II, we first present the mathematical model for the incompressible thermal flow under the Boussinesq approximation, followed by the lattice Boltzmann method to obtain velocity and temperature fields. In Sec. III, we first present general features of four different Nusselt numbers, and then analyze the cross-correlation between the Nu and the energy of Fourier mode, the cross-correlation between Nu and the amplitude of POD mode, as well as the ensemble-averaged Nu during flow reversal. In Sec. IV, the main conclusions of the present work are summarized.

II. NUMERICAL METHOD

A. Direct numerical simulation of turbulent thermal convection

We consider incompressible thermal flows under the Boussinesq approximation. The temperature is treated as an active scalar, and its influence on the velocity field is realized through the buoyancy term. The viscous heat dissipation and compression work are neglected, and all the transport coefficients are assumed to be constants. The governing equations can be written as

$$\nabla \cdot \mathbf{u} = 0 \quad (2a)$$

$$\frac{\partial \mathbf{u}}{\partial t} + \mathbf{u} \cdot \nabla \mathbf{u} = -\frac{1}{\rho_0} \nabla p + \nu \nabla^2 \mathbf{u} + g\beta(T - T_0)\hat{\mathbf{z}} \quad (2b)$$

$$\frac{\partial T}{\partial t} + \mathbf{u} \cdot \nabla T = \kappa \nabla^2 T \quad (2c)$$

where $\mathbf{u} = (u, w)$ is the fluid velocity. p and T are the pressure and temperature of the fluid, respectively. ρ_0 and T_0 are the reference density and temperature, respectively. $\hat{\mathbf{z}}$ is the unit vector in the vertical direction. We study the flow and heat transfer in a 2D cell for two reasons. First, the computational cost for 2D simulations is much lower than that of the 3D simulations, thus, we can adopt a fine resolution of the boundary layers to capture the extreme events at high Rayleigh numbers. Secondly, a particular configuration of choice in the experimental studies is the quasi-2D rectangular geometry, which enables the minimization or even elimination of the influence from the three-dimensional dynamic features of the large-scale circulation. To efficiently mimic the quasi-2D rectangular cell adopted in the experiment, we choose the 2D cell in the numerical simulation.

We adopt the lattice Boltzmann (LB) method^{31–34} as the numerical tool for DNS of turbulent thermal convection, instead of directly solving the discretized nonlinear partial differential equations. The advantages of the LB method include easy implementation and parallelization, particularly on heterogeneous computing platforms such as GPUs³⁵. The LB model to solve fluid flows and heat transfer is based on the double distribution function approach, which consists of a D2Q9 model for the Navier-Stokes equations (i.e., Eqs. 1a and 1b) to simulate fluid flows and a D2Q5 model for the convection-diffusion equations (i.e., Eq. 1c) to simulate heat transfer. In the LB method, to solve Eqs. 1a and 1b, the evolution equation of the density distribution function is written as

$$f_i(\mathbf{x} + \mathbf{e}_i \delta_t, t + \delta_t) - f_i(\mathbf{x}, t) = -(\mathbf{M}^{-1} \mathbf{S})_{ij} \left[\mathbf{m}_j(\mathbf{x}, t) - \mathbf{m}_j^{(\text{eq})}(\mathbf{x}, t) \right] + \delta_t F'_i \quad (3)$$

where f_i is the density distribution function. \mathbf{x} is the fluid parcel position, t is the time, and δ_t is the time step. \mathbf{e}_i is the discrete velocity along the i th direction. \mathbf{M} is the orthogonal transformation matrix that projects the density distribution function f_i and its equilibrium $f_i^{(\text{eq})}$ from the velocity space onto the moment space as $\mathbf{m} = \mathbf{M}\mathbf{f}$ and $\mathbf{m}^{(\text{eq})} = \mathbf{M}\mathbf{f}^{(\text{eq})}$. \mathbf{S} is the diagonal relaxation matrix and F_i' is the forcing term. The macroscopic density ρ and velocity \mathbf{u} are obtained from $\rho = \sum_{i=0}^8 f_i$ and $\mathbf{u} = (\sum_{i=0}^8 \mathbf{e}_i f_i + \mathbf{F}/2) / \rho$, where $\mathbf{F} = \rho g \beta (T - T_0) \hat{\mathbf{z}}$. To solve Eq. 2c, the evolution equation of temperature distribution function is written as

$$g_i(\mathbf{x} + \mathbf{e}_i \delta_t, t + \delta_t) - g_i(\mathbf{x}, t) = -(\mathbf{N}^{-1} \mathbf{Q})_{ij} \left[\mathbf{n}_j(\mathbf{x}, t) - \mathbf{n}_j^{(\text{eq})}(\mathbf{x}, t) \right] \quad (4)$$

where g_i is the temperature distribution function. \mathbf{N} is the orthogonal transformation matrix that projects the temperature distribution function g_i and its equilibrium $g_i^{(\text{eq})}$ from the velocity space onto the moment space as $\mathbf{n} = \mathbf{N}\mathbf{g}$ and $\mathbf{n}^{(\text{eq})} = \mathbf{N}\mathbf{g}^{(\text{eq})}$. \mathbf{Q} is the diagonal relaxation matrix. The macroscopic temperature T is obtained from $T = \sum_{i=0}^4 g_i$. More numerical details on the LB method and validation of the in-house DNS code can be found in our previous work^{36–38}.

B. Simulation settings

The top and bottom walls of the convection cell are kept at constant cold and hot temperatures, respectively; while the other two vertical walls are adiabatic. All four walls impose no-slip velocity boundary condition. The dimension of the cell is $H \times H$. Simulation results are provided for the Rayleigh number of $10^7 \leq Ra \leq 10^9$, and fixed Prandtl number of $Pr = 5.3$. After reaching statistically stationary state, we take another time span of t_{avg} to obtain statistically convergent results for turbulent analysis. In Table I, we list the t_{avg} both in free-fall time unit $t_f = \sqrt{H/(g\beta\Delta T)}$ and large-eddy turnover time unit $t_E \approx 4\pi/\langle |\omega_c(t)| \rangle_t$, with ω_c denoting the vorticity at the cell center. Because flow reversal occurs frequently at $Ra = 10^8$, to have enough statistics for the reversal events at $Ra = 10^8$, we simulate as long as 480 000 t_f , which enables us to identify 694 flow reversal events. We check whether the grid spacing Δ_g and time interval Δ_t is properly resolved by comparing with the Kolmogorov and Batchelor scales. Here, the Kolmogorov length scale³⁹ is estimated by the global criterion $\eta_K = (v^3/\langle \epsilon_u \rangle)^{1/4} = HPr^{1/2}/[Ra(Nu - 1)]^{1/4}$, the Batchelor length scale^{40,41} is estimated by $\eta_B = \eta_K Pr^{-1/2}$, and the Kolmogorov time scale³⁹ is estimated as $\tau_\eta = \sqrt{v/\langle \epsilon_u \rangle} = t_f \sqrt{Pr/(Nu - 1)}$. We use the volume-averaged Nu_{vol} to estimate the spatial and temporal resolutions, because the other three definitions of Nusselt numbers give

very similar values of Nu , as discussed in Sec. III A. From Table I, we can see that grid spacings satisfy $\max(\Delta_g/\eta_K, \Delta_g/\eta_B) \leq 0.46$ and the time intervals satisfy $\Delta_t \leq 0.00034\tau_\eta$, which ensure the spatial and temporal resolution of the DNS.

TABLE I. Spatial and temporal resolutions of the simulations.

Ra	Pr	Mesh size	Δ_g/η	Δ_g/η_B	Δ_t/τ_η	t_{avg}/t_f	t_{avg}/t_E
10^7	5.3	257^2	0.18	0.41	3.43×10^{-4}	240,000	17,622
10^8	5.3	513^2	0.19	0.44	2.46×10^{-4}	480,000	25,229
10^9	5.3	1025^2	0.20	0.46	1.74×10^{-4}	10,000	1,076

III. RESULTS AND DISCUSSION

A. General features of Nusselt numbers

To have a general understanding of the features for the four different Nusselt numbers, we plot the time series of instantaneous Nusselt numbers at $Ra = 10^7$ and $Pr = 5.3$ for the period of 10 000 free-fall time. From Fig. 1, we can see that all the four time series have similar mean values over time, which is consistent with previous findings that different approaches to calculate the Nusselt numbers would give consistent mean values, as introduced in Sec. I. On the other hand, the volume-averaged Nu_{vol} has the most significant fluctuation, while the wall-averaged Nu_{wall} has the smallest fluctuation. As for the kinetic energy dissipation based $Nu_{kinetic}$ and thermal energy dissipation based $Nu_{thermal}$, the fluctuation in the former values is larger than that in the latter one. We can understand that as the velocity field is more intensely varied compared to the temperature field, leading to stronger temporal fluctuations in the Nu_{vol} and the $Nu_{kinetic}$ that include the velocity field information.

We further check the probability density functions (PDFs) of the four Nusselt numbers. In Fig. 2, we show the PDFs of the normalized Nusselt numbers $(Nu - \mu_{Nu})/\sigma_{Nu}$. Here, μ_{Nu} and σ_{Nu} represent the mean value and standard deviation of the Nu . Generally, the distributions of the normalized Nu are universe and all profiles of the PDFs collapse onto a single curve. However, we should also note the differences in the distributions of PDFs for flows with different Ra . At $Ra = 10^7$ and $Ra = 10^8$, the distribution is asymmetric (right-skewed) and can be described by the Gamma distribution or generalized extreme value (GEV) distribution; in contrast, at $Ra = 10^9$, the

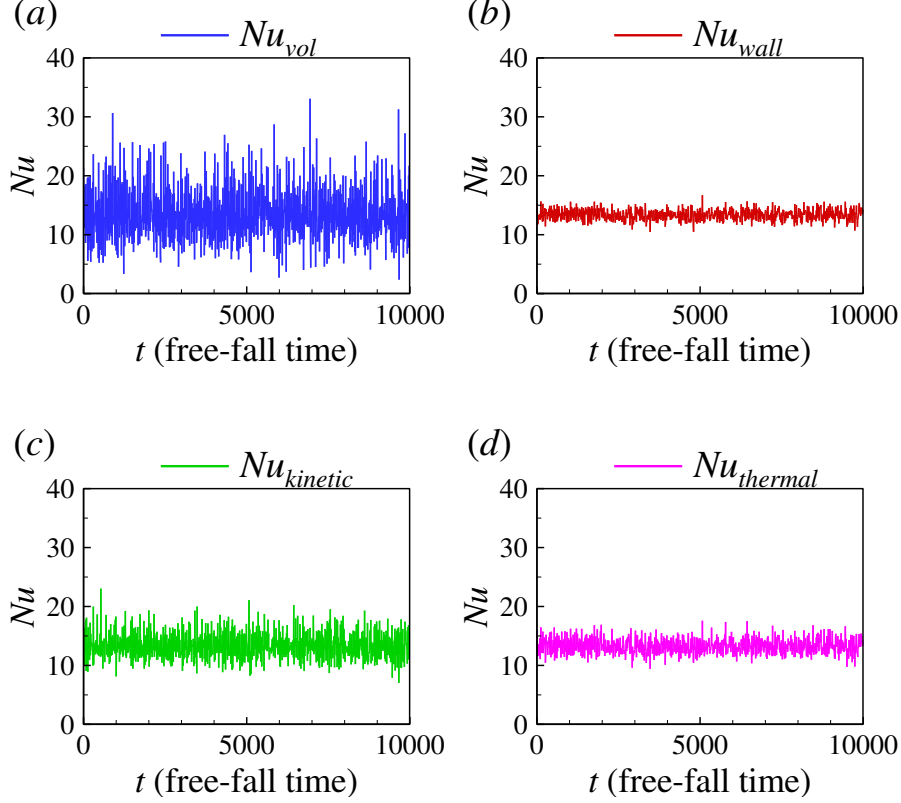


FIG. 1. Time series of instantaneous Nusselt numbers: (a) the volume-averaged Nu_{vol} , (b) the wall-averaged Nu_{wall} , (c) the kinetic energy dissipation based $Nu_{kinetic}$, and (d) the thermal energy dissipation based $Nu_{thermal}$ at $Ra = 10^7$ and $Pr = 5.3$.

distribution is symmetric and can be described by the Gaussian distribution. A possible reason is that at $Ra = 10^7$ and $Ra = 10^8$, the LSC is unstable and reverses its direction frequently, the erratic behavior of the LSC leads to the fluctuations of the Nu with more extreme events⁴². At $Ra = 10^9$, the LSC is much more stable, the random fluctuations of the Nu follows the Gaussian distribution.

We quantitatively evaluate the mean and root-mean-square (r.m.s.) values of the four instantaneous Nusselt numbers, as shown in Table II. We also provide the reference results from Zhang et al.⁴³ with the same simulation settings (denoted as Nu_{ref}). The relative difference can be calculated as $|\langle Nu_i \rangle_t - Nu_{ref}| / Nu_{ref}$ with $i \in \{vol, wall, kinetic, thermal\}$, and the differences are included in brackets in the corresponding rows. From Table II, we can see that the differences in Nusselt numbers are within 1%, indicating that our results are consistent with the previous one. On the other hand, we can see in the present simulations, the Nusselt numbers calculated from four different

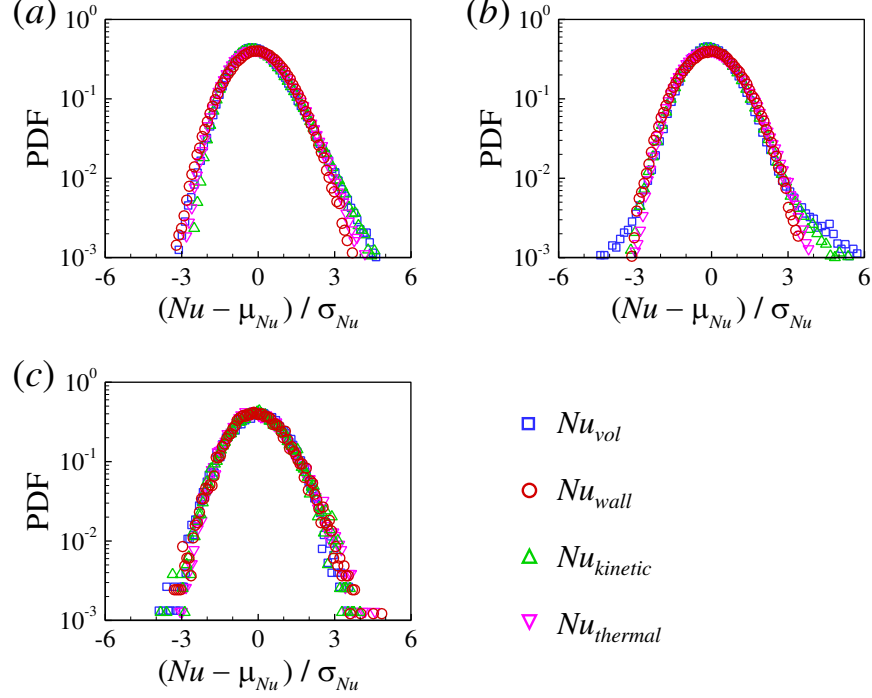


FIG. 2. Probability density functions (PDFs) of the normalized Nusselt numbers $(Nu - \mu_{Nu}) / \sigma_{Nu}$ at (a) $Ra = 10^7$, (b) $Ra = 10^8$, and (c) $Ra = 10^9$.

approaches show good consistency with each other. We also calculate the ratio between the r.m.s. and the mean value of the Nusselt numbers to measure their relative fluctuation as $\sigma_{Nu_i} / \langle Nu_i \rangle_t$, and the results are included in the brackets in the corresponding rows. At higher Ra , there are more extreme events, yet occur at thinner boundary layers. Thus, with the increase of the Ra , the r.m.s. of the Nu increases while its relative fluctuation decreases. Overall, the relative fluctuation is significantly larger for the Nu_{vol} than that for the Nu_{wall} .

We then examine the flow and temperature fields when the instantaneous Nu reaches 'extreme' large or small values, namely, the instant when $Nu(t) > (\langle Nu \rangle + 3\sigma_{Nu})$ or $Nu(t) < (\langle Nu \rangle - 3\sigma_{Nu})$. In Fig. 3, the top panel shows typical snapshots of temperature field and streamlines when the instantaneous Nu reaches 'extreme' large value, while the bottom panel shows snapshots when the Nu reaches 'extreme' small value. We can see that at $Ra = 10^7$ and 10^8 , the flow structures change significantly for these two states. Specifically, when $Nu(t) > (\langle Nu \rangle + 3\sigma_{Nu})$, there exist two vertically stacked rolls, the thermal plumes rising from the hot bottom wall almost vertically hit the opposite wall. When $Nu(t) < (\langle Nu \rangle - 3\sigma_{Nu})$, there exist two horizontally stacked rolls, the plumes that are rising along the vertical wall lose their kinetic energy at half-height and then exhibit

TABLE II. The mean and root-mean-square (r.m.s.) values of Nusselt numbers. Data included in the brackets represent the relative difference of the Nusselt number as $|\langle Nu_i \rangle_t - Nu_{\text{ref}}|/Nu_{\text{ref}}$ or the relative fluctuation of the Nusselt number as $\sigma_{Nu_i}/\langle Nu_i \rangle_t$, where $i \in \{\text{vol}, \text{wall}, \text{kinetic}, \text{thermal}\}$.

Ra	10^7	10^8	10^9
Nu_{ref} (Ref. 43)	13.28	26.21	51.28
$\langle Nu_{\text{vol}} \rangle_t$	13.36 (0.60%)	26.36 (0.57%)	51.53 (0.49%)
$\langle Nu_{\text{wall}} \rangle_t$	13.37 (0.68%)	26.38 (0.65%)	51.57 (0.57%)
$\langle Nu_{\text{kinetic}} \rangle_t$	13.31 (0.23%)	26.30 (0.34%)	51.46 (0.35%)
$\langle Nu_{\text{thermal}} \rangle_t$	13.29 (0.08%)	26.23 (0.08%)	51.31 (0.06%)
$\sigma_{Nu_{\text{vol}}}$	4.43 (33.2%)	8.56 (32.5%)	12.17 (23.6%)
$\sigma_{Nu_{\text{wall}}}$	0.88 (6.6%)	1.66 (6.3%)	1.88 (3.7%)
$\sigma_{Nu_{\text{kinetic}}}$	2.23 (16.8%)	3.24 (12.3%)	3.52 (6.8%)
$\sigma_{Nu_{\text{thermal}}}$	1.30 (9.8%)	2.22 (8.5%)	2.68 (5.2%)

horizontal motion. Thus, here we provide direct evidence that heat transfer is on average efficient with the two vertically stacked rolls, while it is on average inefficient with the two horizontally stacked rolls. At $Ra = 10^9$, the flow structure remains a stable big roll, which is nearly independent of the variation of the Nu .

B. Cross-correlation between Nusselt numbers and the Fourier mode of the flow

The Fourier mode decomposition has been employed to study flow reversal mechanisms in 2D and quasi-2D square convection cells^{24,27,28,44–47}, as well as heat transfer properties in quasi-2D cell^{48,49}. Specifically, the instantaneous velocity field (u, w) is projected onto the Fourier basis $(\hat{u}^{m,n}, \hat{w}^{m,n})$ as

$$u(x, z, t) = \sum_{m,n} A_x^{m,n}(t) \hat{u}^{m,n}(x, z) \quad (5a)$$

$$w(x, z, t) = \sum_{m,n} A_z^{m,n}(t) \hat{w}^{m,n}(x, z) \quad (5b)$$

Here, the Fourier basis $(\hat{u}^{m,n}, \hat{w}^{m,n})$ is chosen as^{27,28}

$$\hat{u}^{m,n}(x, z) = 2 \sin(m\pi x) \cos(n\pi z) \quad (6a)$$

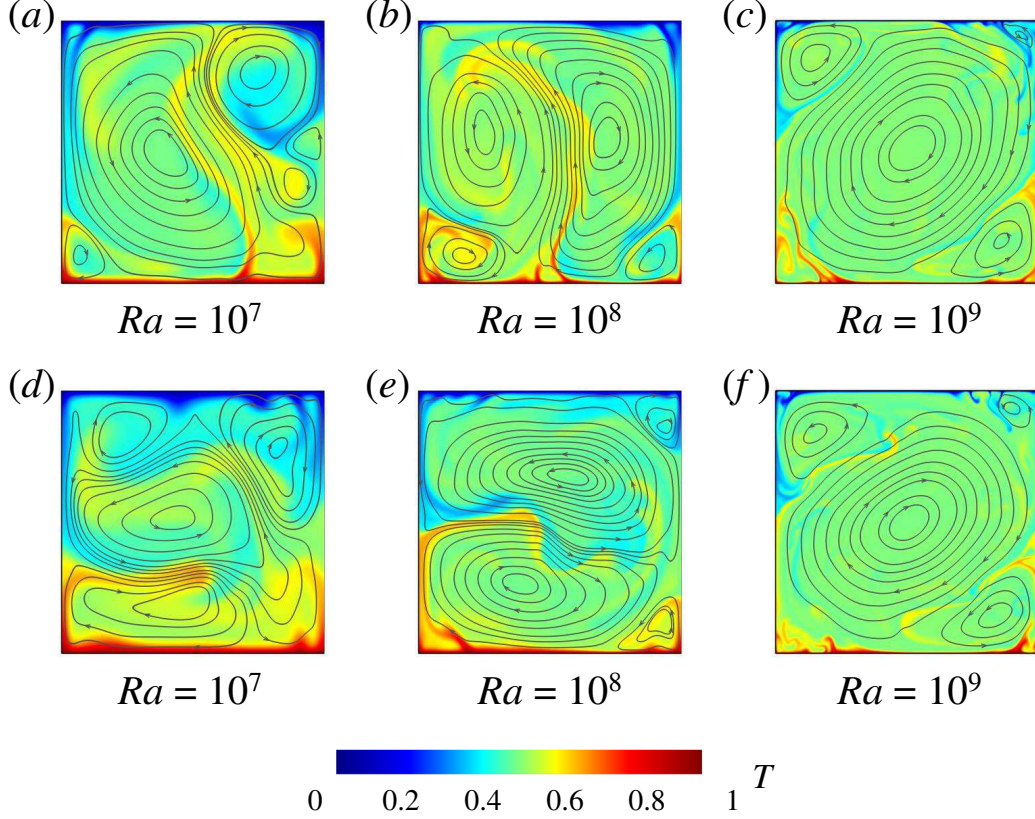


FIG. 3. Typical snapshots of temperature field and streamlines when the instantaneous Nu reaches (a-c) 'extreme' large value or (d-f) 'extreme' small value : (a, d) at $Ra = 10^7$, (b, e) at $Ra = 10^8$, (c, f) at $Ra = 10^9$.

$$\hat{w}^{m,n}(x,z) = -2\cos(m\pi x)\sin(n\pi z) \quad (6b)$$

Although the above Fourier basis functions do not satisfy the no-slip velocity boundary condition, it was shown previously that the Fourier mode decomposition capture the convection flow profiles well^{27,28,44}. The instantaneous amplitude of the Fourier mode is then calculated as

$$A_x^{m,n}(t) = \langle u(x,z,t), \hat{u}^{m,n}(x,z) \rangle = \sum_i \sum_j u(x_i, z_j, t) \hat{u}^{m,n}(x_i, z_j) \quad (7a)$$

$$A_z^{m,n}(t) = \langle w(x,z,t), \hat{w}^{m,n}(x,z) \rangle = \sum_i \sum_j w(x_i, z_j, t) \hat{w}^{m,n}(x_i, z_j) \quad (7b)$$

where $\langle u, \hat{u} \rangle$ and $\langle w, \hat{w} \rangle$ denote the inner product of u and \hat{u} , w and \hat{w} , respectively. The energy in each Fourier mode⁴⁸ is evaluated as $E^{m,n}(t) = \sqrt{[A_x^{m,n}(t)]^2 + [A_z^{m,n}(t)]^2}$. Here, the (m,n) Fourier mode corresponds to a flow structure with m rolls in the x -direction and n rolls in the z -direction, as illustrated in Fig. 4. In the following, we will consider m and $n = 1, 2, 3$, namely the first nine Fourier modes.

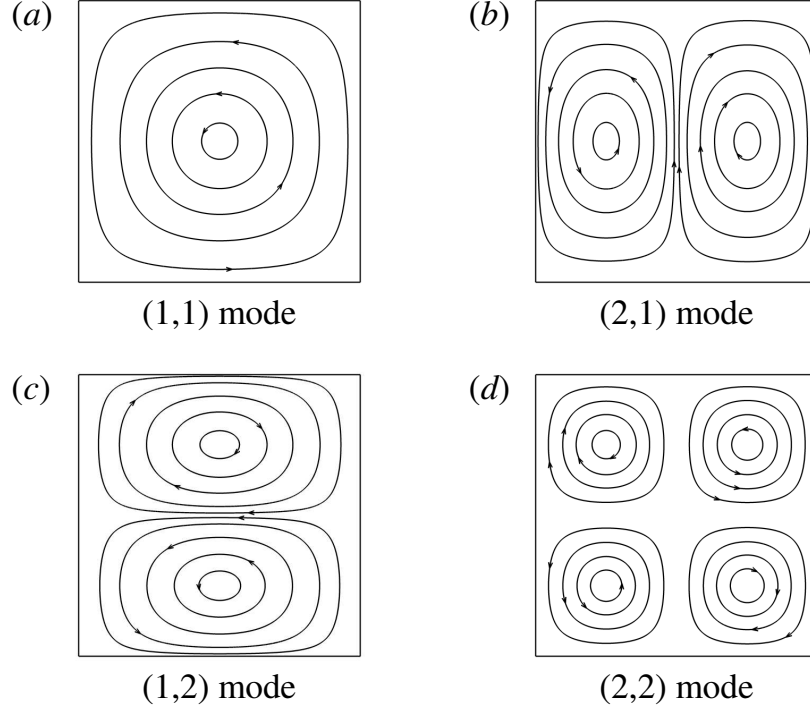


FIG. 4. Schematically illustration of the first four Fourier modes: (a) the (1,1) mode, (b) the (2,1) mode, (c) the (1,2) mode, and (d) the (2,2) mode.

The time evolution of energy in each Fourier mode at $Ra = 10^7$ and $Ra = 10^9$ for the period of 10,000 free-fall time are plotted in Figs. 5(a) and 5(b), respectively. Here, we normalize energy of the (m,n) Fourier mode $E^{m,n}(t)$ by dividing the total energy $E_{total}(t) = \sum_{m,n} E^{m,n}(t)$. We can see that for both Ra , the dominant Fourier mode is the (1,1) mode because it accounts for over 40% of the total energy. We can understand this flow mode as the primary roll in the cell center, corresponding to the large-scale circulation of the flow. The time-averaged energy in each Fourier mode $\langle E^{m,n}(t)/E_{total}(t) \rangle_t$ as functions of Ra is further plotted in Fig. 5(c). At $Ra = 10^9$, the large-scale roll is of a tilde elliptical shape and it does not concentrate near the perimeter of the cell⁵⁰, thus the relative contribution from the (1,1) mode is the small and the two corner rolls account much more energy than they do in other Ra . We also notice that in Figs. 5(a) and 5(b), the evolutions of the (1,1) mode fluctuate more intense at $Ra = 10^7$ than that at $Ra = 10^9$. We then calculate the stability of the (1,1) Fourier mode⁴⁷ as $S^{1,1} = \langle E^{1,1} \rangle / \sigma_{E^{1,1}}$, such that a larger value of $S^{1,1}$ indicates a more stable main roll. We can see from Fig. 5(d) that the stability of the (1,1) mode is weak at $Ra = 10^7$ and 10^8 , which is due to flow reversal of the main roll. Since the flow reversal is more frequent at $Ra = 10^8$ compared with that at $Ra = 10^7$, the $S^{1,1}$ is smaller at the

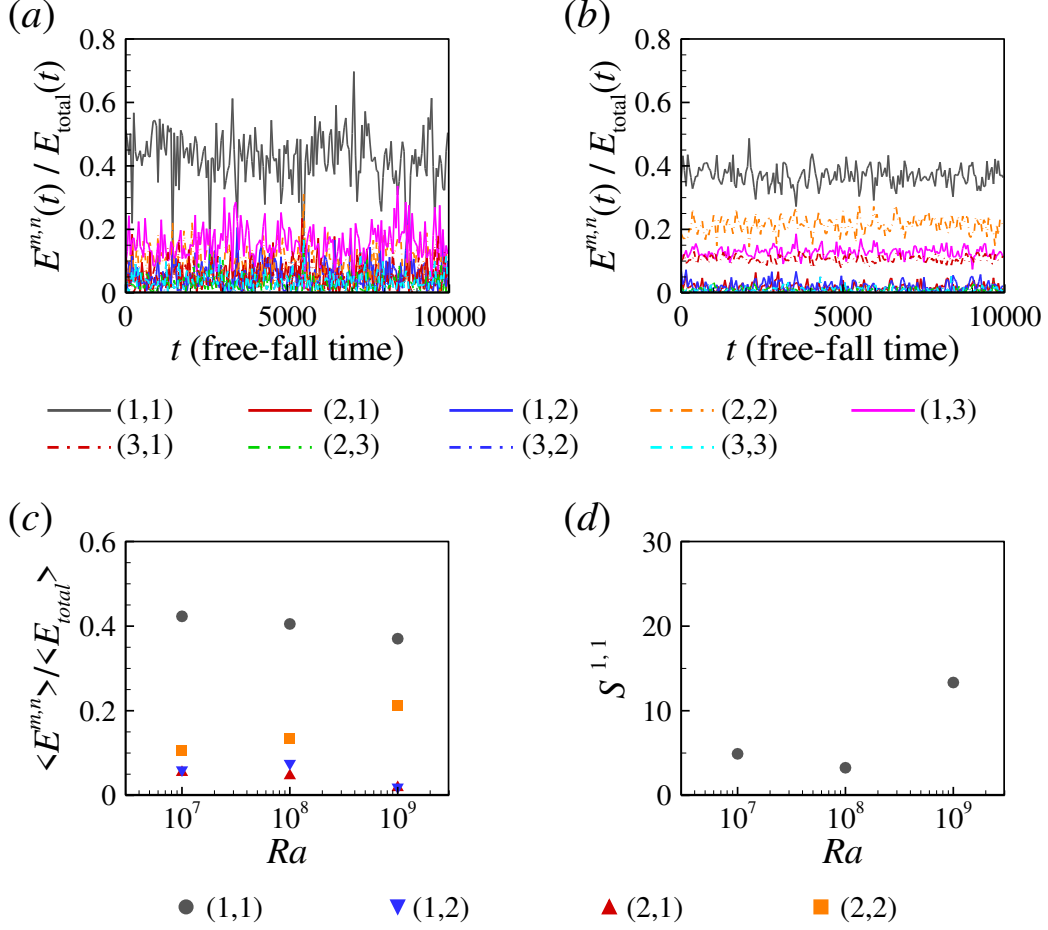


FIG. 5. The time evolution of the energy in each Fourier mode for (a) $Ra = 10^7$ and (b) $Ra = 10^9$; (c) the time-averaged energy in each Fourier mode as functions of the Ra ; (d) the stability of the (1,1) mode as functions of the Ra .

former Ra . In contrast, the main roll is much more stable at $Ra = 10^9$, which is consistent with the observations shown in Fig. 3.

To examine the abilities of four different Nusselt numbers on revealing connections between heat transfer efficiency and internal flow structures, we calculate the cross-correlation between the Nu and the energy of the (m,n) Fourier mode $E^{m,n}$ as $R_{Nu,E^{m,n}}(\tau) = \langle (Nu(t+\tau) - \langle Nu \rangle)(E^{m,n}(t) - \langle E^{m,n} \rangle) \rangle / (\sigma_{Nu} \sigma_{E^{m,n}})$, where σ_{Nu} and $\sigma_{E^{m,n}}$ are the standard deviation of the Nu and the $E^{m,n}$, respectively. In Fig. 6, we plot the cross-correlation function as functions of dimensionless time delay τ/t_E at $Ra = 10^7$ and $Pr = 5.3$. Overall, we observe periodicity in the cross-correlation between instantaneous Nu and energies of the (1,1) and (2,2) Fourier modes, which is due to the periodicity of these flow modes. From Fig. 6(a), we can see that the volume-averaged Nu_{vol}

and the energy of the $(1, 1)$ Fourier mode $E^{1,1}$ show a strong positive correlation. Similarly, the kinetic energy dissipation based Nu_{kinetic} show a positive correlation with the $E^{1,1}$ as that of the Nu_{vol} , but only with a time lag of $\tau \approx 0.3 t_E$. On the other hand, the positive correlation of wall-averaged Nu_{wall} and $E^{1,1}$ is weaker compared with that of Nu_{vol} and Nu_{kinetic} . The thermal energy dissipation based Nu_{thermal} follows a similar pattern with the Nu_{wall} on the correlations with $E^{1,1}$. Previous results^{19,20,22,23} have suggested that heat transfer is more efficient with the single-roll flow structure on average, which corresponds to the $(1, 1)$ Fourier mode. Thus, the correlations of the Nu_{vol} and the Nu_{kinetic} with the $E^{1,1}$ shown here can reproduce previous findings better than the Nu_{wall} and the Nu_{thermal} . The possible reason is that both the Nu_{vol} and the Nu_{kinetic} contain velocity field information, while the flow structure obtained via Fourier flow mode analysis is also essentially based on velocity field information. In contrast, the Nu_{wall} and the Nu_{thermal} only contain temperature field information, and they may not be good candidate to reveal the connections between heat transfer efficiency and internal flow structures. In Fig. 6(b), we can see that all four Nusselt numbers show positive correlations with the $E^{2,1}$, suggesting that the $(2, 1)$ Fourier mode (corresponding to two horizontally stacked rolls) is efficient for heat transfer on average, while the only difference lies in the time lag. In Fig. 6(c), all the Nusselt numbers show negative correlations with the $E^{1,2}$, suggesting that the $(1, 2)$ Fourier mode (corresponding to two vertically arranged rolls) is inefficient for heat transfer on average. Again, the difference lies in the time lag. Finally, for the $(2, 2)$ Fourier mode, its energy is positively correlated with all the Nusselt numbers at time, suggesting the quadrupolar flow is efficient for heat transfer on average.

C. Cross-correlation between Nusselt numbers and the amplitude of POD mode

The proper orthogonal decomposition (POD) has been employed to study flow reversal mechanisms in both 2D and 3D convection cells^{51–54}. In the POD^{29,30}, the spatio-temporal vector field $\mathbf{X}(\mathbf{r}, t)$ is decomposed as a superposition of empirical orthogonal eigenfunctions $\phi_i(\mathbf{r})$ and their amplitudes $a_i(t)$ as

$$\mathbf{X}(\mathbf{r}, t) = \sum_{i=1}^{\infty} a_i(t) \phi_i(\mathbf{r}) \quad (8)$$

The eigenfunctions $\phi_i(\mathbf{r})$ are solutions of the eigenvalue problem

$$\int_{\Omega} \left[\frac{1}{N} \sum_{k=1}^N \mathbf{X}(\mathbf{r}, t_k) \mathbf{X}(\mathbf{r}', t_k) \right] \phi_i(\mathbf{r}') d\mathbf{r}' = \lambda_i \phi_i(\mathbf{r}) \quad (9)$$

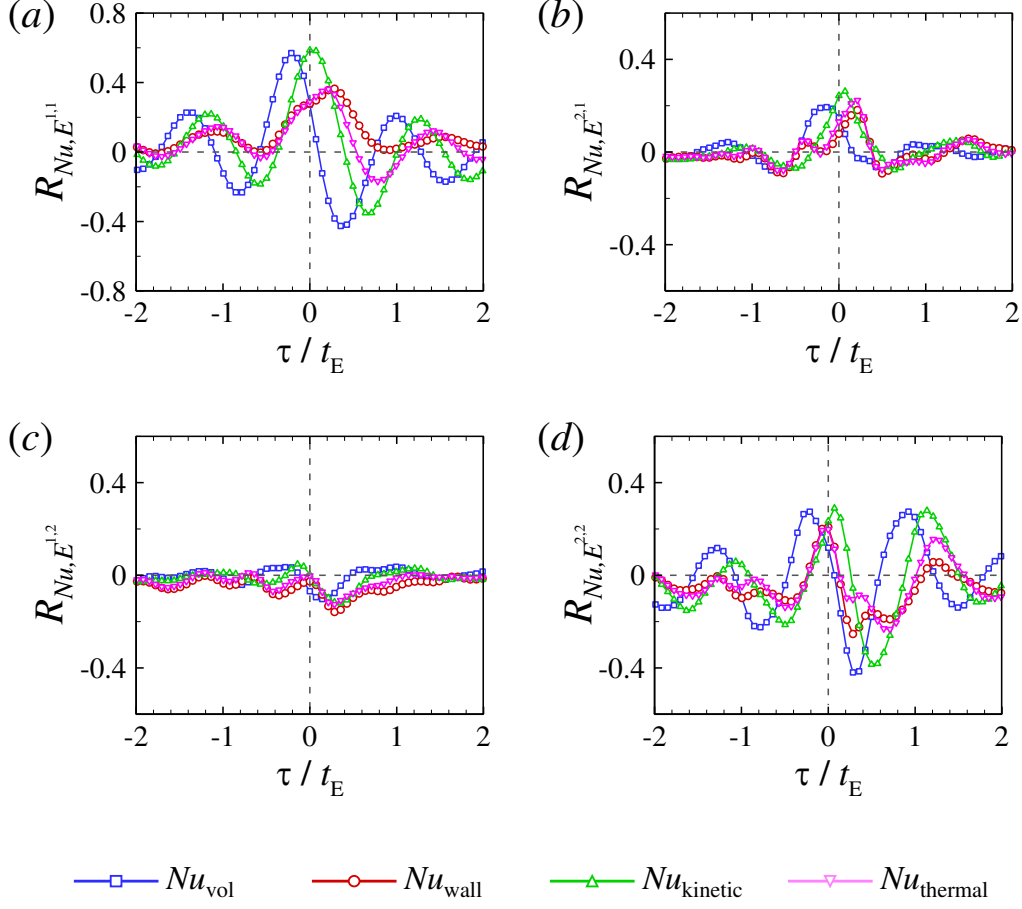


FIG. 6. Cross-correlation between the instantaneous Nu and the energy of (a) the Fourier (1, 1) mode, (b) the Fourier (2, 1) mode, (c) the Fourier (1, 2) mode, and (d) the Fourier (2, 2) mode at $Ra = 10^7$ and $Pr = 5.3$.

where Ω is the spatial domain, and N is the total snapshots. If the empirical eigenfunctions are normalized, we have $\langle a_i(t)a_j(t) \rangle_t = \delta_{ij}\lambda_i$, where δ_{ij} is Kroneker symbol and λ_i is the energy of the i th POD mode. The eigenvalue problem described in Eq. 9 can also be written as

$$\mathbf{C}\Phi = \Phi\Lambda \quad (10)$$

where the positive definite symmetric matrix $\mathbf{C} = (1/N)\mathbf{X}\mathbf{X}^T$ is the auto-correlation matrix of \mathbf{X} . The columns ϕ_i of the matrix Φ are the eigenvectors of matrix \mathbf{C} corresponding to the eigenvalues λ_i . The matrix Λ is a diagonal matrix containing these eigenvalues.

On the other hand, the singular value decomposition (SVD) algorithm provides a numerically stable matrix decomposition that is guaranteed to exist^{55,56}. Generally, for the dataset $\mathbf{X} \in \mathbb{R}^{n \times m}$, we have $\mathbf{X} = \mathbf{U}\Sigma\mathbf{V}^T$, where $\mathbf{U} \in \mathbb{R}^{n \times n}$ and $\mathbf{V} \in \mathbb{R}^{m \times m}$ are unitary matrices, and their components

are denoted as \mathbf{u}_i and \mathbf{v}_i , respectively. $\Sigma = \text{diag}(\sigma_1, \sigma_2, \dots, \sigma_m)$ is a diagonal matrix containing real and non-negative entries, and these diagonal elements are singular values of matrix \mathbf{X} . The SVD is closely related to the eigenvalue problem involving the correlation matrix \mathbf{C} . The relation $\mathbf{X}\mathbf{X}^T = \mathbf{U}\Sigma\Sigma^T\mathbf{U}^T$ indicates that the solution of the eigenvalue problem described in Eq. 10 can be solved with the SVD algorithm, where the eigenvector is $\Phi = \mathbf{U}$ and the eigenvalue is $\Lambda = (1/N)\Sigma\Sigma^T$. We then have the POD mode ϕ_i , its energy λ_i , and its the amplitude $a_i(t)$ as

$$\phi_i(\mathbf{r}) = \mathbf{u}_i, \quad \lambda_i = \frac{1}{N}\sigma_i^2, \quad a_i(t) = \sigma_i\mathbf{v}_i \quad (11)$$

The shape of the first four POD modes is shown in Fig. 7, which was obtained on a dataset of 10,000 snapshots at $Ra = 10^7$ and $Pr = 5.3$. The most energetic POD mode consists of a primary roll in the cell center, which is similar to the (1,1) Fourier mode. The second most energetic POD mode is associated with a quadrupolar flow, which corresponds to the (2,2) Fourier mode. The third most energetic POD mode consists of two rolls stacked in the vertical direction, and it corresponds to the (1,2) Fourier mode. The fourth most energetic POD mode consists of two rolls stacked in the horizontal direction, and it corresponds to the (2,1) Fourier mode. Thus, the leading POD modes are directly related to the Fourier modes.

The time evolution of each POD mode amplitude at $Ra = 10^7$ and $Pr = 5.3$ for the period of 10,000 free-fall time is plotted in Fig. 8(a). We can see that the amplitude of the first POD mode changes its sign at $t \approx 5500 t_f$, which suggests a flow reversal event because the first POD mode is related to the large-scale circulation roll. Overall, the amplitude of the first POD mode is much larger than the rest ones, which can also be demonstrated from the accumulated energy $\sum \lambda_i$ as functions of POD mode number i . In Fig. 8(b), we can see that the first POD mode accounts for over 77% of the total energy. The dashed-gray line in Fig. 8(b) indicates that it takes fifty POD modes to reach 99% of the total energy.

To further examine the abilities of four different Nusselt numbers on revealing connections between heat transfer efficiency and internal flow structures, we then calculate the cross-correlation between the Nu and the absolute value of POD mode amplitude $|a_i|$ as $R_{Nu,|a_i|}(\tau) = \langle (Nu(t + \tau) - \langle Nu \rangle)(|a_i(t)| - \langle |a_i| \rangle) \rangle / (\sigma_{Nu}\sigma_{|a_i|})$, where σ_{Nu} and $\sigma_{|a_i|}$ are the standard deviation of the Nu and the $|a_i|$, respectively. Here, we adopt the absolute value of the POD mode amplitude, since the change of its sign only indicates the reversal of the flow circulation direction. In Fig. 9, we plot the cross-correlation function as functions of time delay τ at $Ra = 10^7$ and $Pr = 5.3$. Following the analysis on the correlation between the Nu and the energy of the Fourier mode $E^{m,n}$

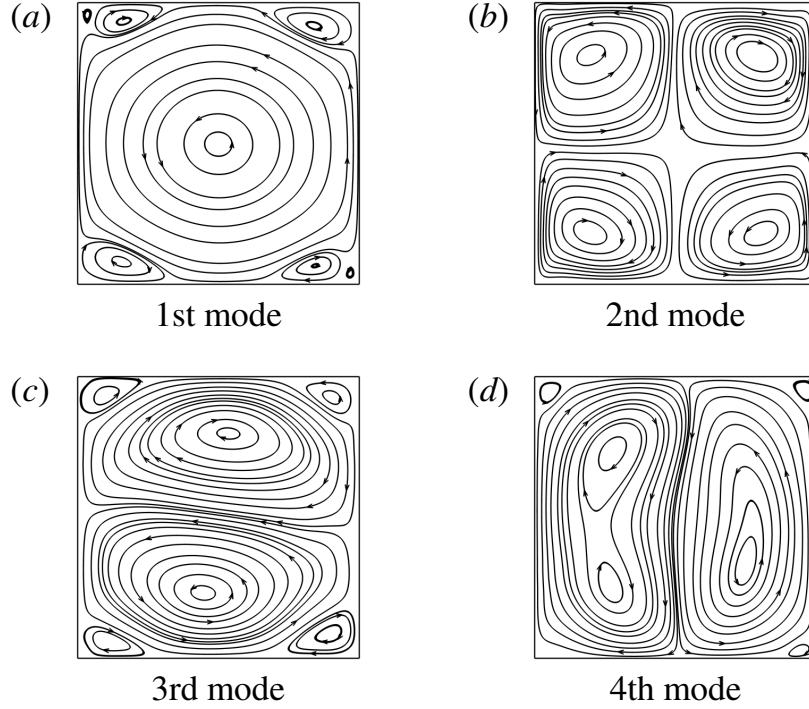


FIG. 7. (a-d) The first four proper orthogonal decomposition (POD) modes at $Ra = 10^7$ and $Pr = 5.3$ for the period of 10,000 free-fall time.

(see Sec. III B), we can generally perform the same analysis on the correlation between the Nu and the absolute value of the POD mode amplitude $|a_i|$. For the sake of clarity, we will not repeat the detailed procedure here. The main conclusion we can draw from results in Figs. 6 and 9 is that the POD mode dynamics exhibits almost the same behavior as that of the Fourier mode. We can observe one-to-one correspondence in terms of the cross-correlation functions between the above two different flow mode analysis approaches. Thus, the POD analysis further justify that using the Nu_{vol} and $Nu_{kinetic}$ can better reproduce the correlation between heat transfer efficiency and flow structure obtained via flow mode analysis, and the use of these two Nusselt numbers is recommended.

D. Ensemble-averaged Nusselt numbers during flow reversal

With long-time DNS, we identified a large number of 694 reversal events at $Ra = 10^8$ and $Pr = 5.3$, which allows us to examine the behavior of different Nusselt numbers during flow reversal. Based on the DNS data, we calculate the ensemble-averaged time trace of Nu as follows:

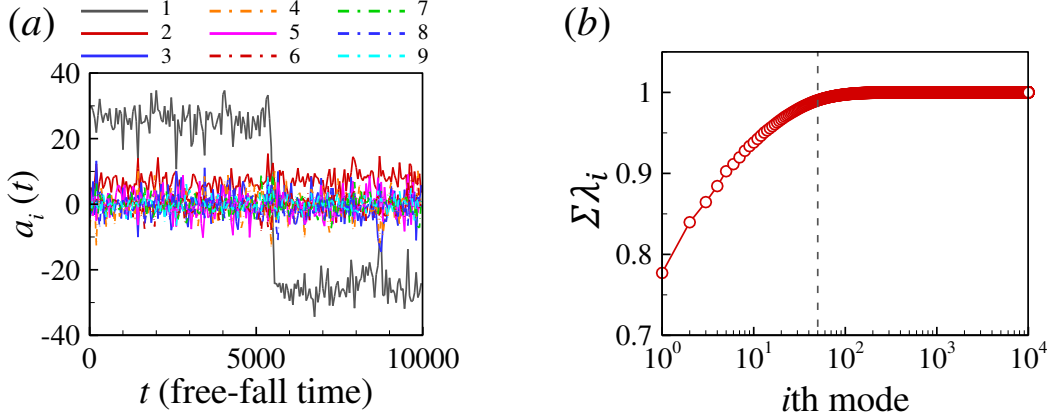


FIG. 8. (a) The time evolution of the absolute value of POD mode amplitude $a_i(t)$, (b) the accumulated energy $\Sigma \lambda_i$ as functions of POD mode number i at $Ra = 10^7$ and $Pr = 5.3$. The dashed-gray line indicates the mode number to reach 99% of the total energy.

we first locate the data point where the dimensionless angular momentum L/L_0 is crossing zero during the reversal. Then, starting from this data point, we go forward and backward for 150 data points respectively, extract this 300 data-point-long time segment of Nu (corresponding to $30 t_E$, which is enough to cover the mean duration time of $16 t_E$ for the flow reversal). After that, we average all the 694 time segments of Nu onto this 300 data points, the so obtained averaged time trace exhibits the ensemble-averaged time evolution of Nu during flow reversals, as shown in Fig. 10. For the wall-averaged Nu_{wall} , the kinetic energy dissipation based Nu_{kinetic} , and the thermal energy dissipation based Nu_{thermal} (see Figs. 10b-10d), we can only observe that the Nu decrease before the reversal, drop to their minima at $t \approx 0$, and then increase to their normal value after the reversal. In contrast, we can observe a momentary overshoot in the volume-averaged Nu_{vol} above its average value (see Fig. 10a) during flow reversal. We note among the four different Nusselt numbers, only the Nu_{vol} simultaneously include the velocity and temperature fields information, while the other three Nu reflect either the velocity field or the temperature field information, which may be the reason that only Nu_{vol} can reproduce the 'overshoot' phenomena observed in previous experimental study²⁴.

IV. CONCLUSIONS

In this work, we have performed high-resolution and long-time direct numerical simulations of turbulent Rayleigh-Bénard convection to investigate the correlation of internal flow structure and

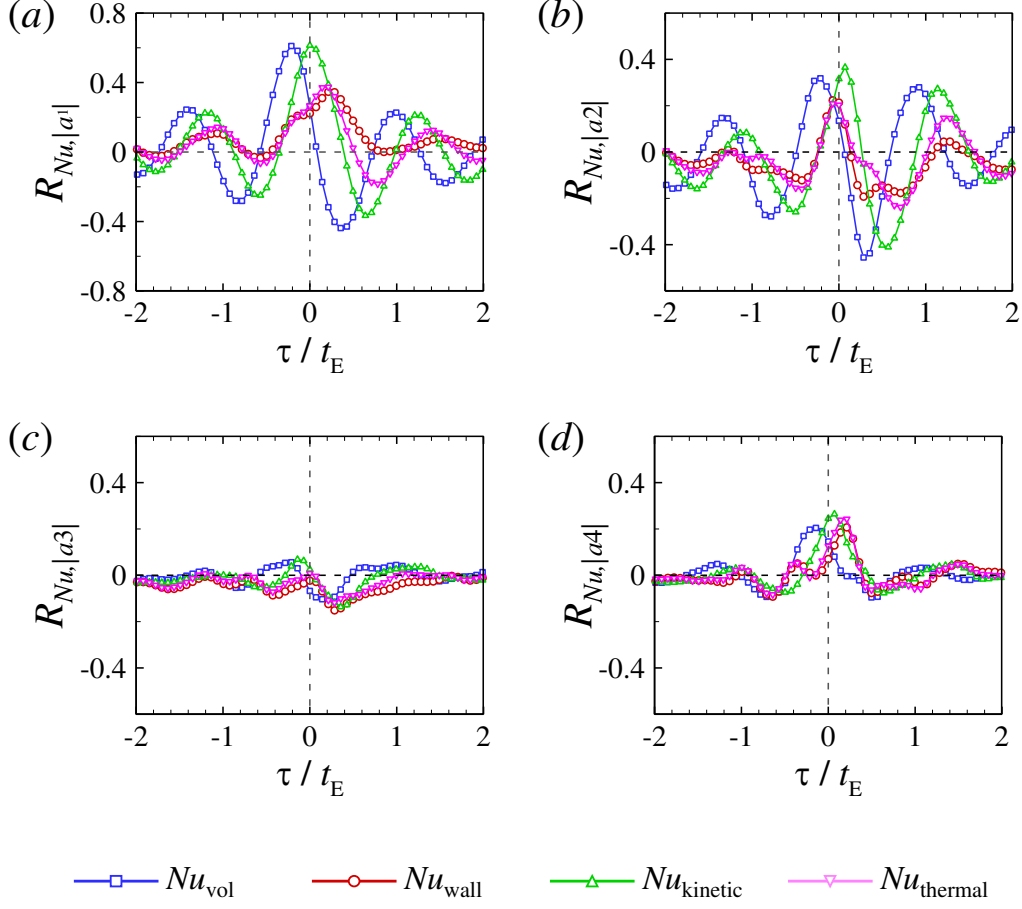


FIG. 9. Cross-correlation between the instantaneous Nu and the amplitude (absolute value) of (a) the first POD mode, (b) the second POD mode, (c) the third POD mode, and (d) the fourth POD mode at $Ra = 10^7$ and $Pr = 5.3$.

heat transfer efficiency. Specifically, we examined the abilities of four different Nusselt numbers (i.e., the volume-averaged Nu_{vol} , the wall-averaged Nu_{wall} , the kinetic energy dissipation based Nu_{kinetic} and the thermal energy dissipation based Nu_{thermal}) on revealing this connection. The main findings are summarized as follows:

1. All the four different Nusselt numbers exhibit consistent time-averaged mean values and their PDFs collapse onto a single curve. The Nu_{vol} shows the largest fluctuation, while the Nu_{wall} shows the smallest fluctuation.
2. The Fourier mode decomposition and the POD analysis show that in the 2D square RB cell, the single-roll flow structure, the horizontally stacked roll flow structure, and the quadrupo-

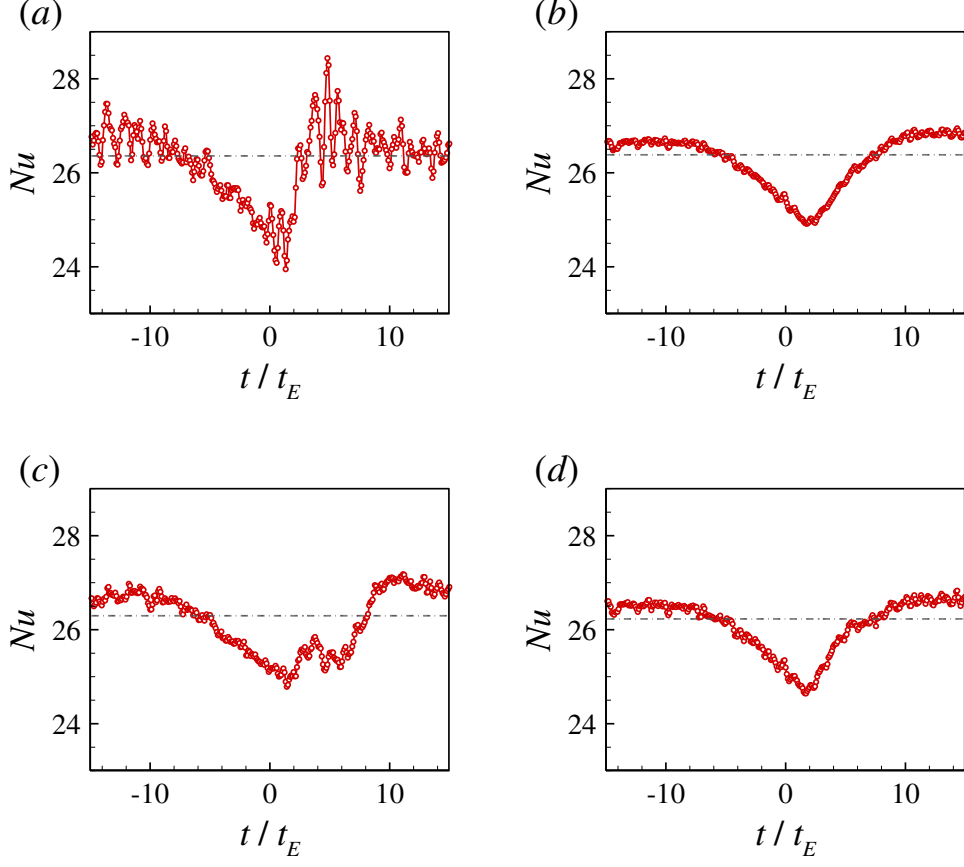


FIG. 10. Ensemble-averaged Nusselt numbers during flow reversal: (a) the volume-averaged Nu_{vol} , (b) the wall-averaged Nu_{wall} , (c) the kinetic energy dissipation based Nu_{kinetic} , and (d) the thermal energy dissipation based Nu_{thermal} at $Ra = 10^8$ and $Pr = 5.3$. The dashed-gray lines indicate the average value of the corresponding Nu .

lar flow structure are more efficient for heat transfer on average. In contrast, the vertically stacked roll flow structure is inefficient for heat transfer on average.

3. The cross-correlation functions between instantaneous Nu and flow mode amplitude indicate that the Nu_{vol} and Nu_{kinetic} can better reproduce the correlation between flow structure and heat transfer efficacy than that of the Nu_{wall} and Nu_{thermal} . To analyze the correlation between the Nu and the flow structures obtained via flow mode analysis, we recommend using the former two Nusselt numbers.
4. During flow reversal, previous experimental study reported that the Nu has a momentary overshoot above its average value due to more coherent flow or plumes. Among the four

Nusselt numbers, only the ensemble-averaged time trace of Nu_{vol} can reproduce the overshoot phenomena.

ACKNOWLEDGMENTS

This work was supported by the National Natural Science Foundation of China (NSFC) through Grant Nos. 11902268 and 11772259, the Fundamental Research Funds for the Central Universities of China (Nos. D5000200570 and 3102019PJ002), and the 111 project of China (No. B17037).

DATA AVAILABILITY STATEMENT

The data that support the findings of this study are available from the corresponding authors upon reasonable request.

REFERENCES

- ¹G. Ahlers, S. Grossmann, and D. Lohse, “Heat transfer and large scale dynamics in turbulent Rayleigh-Bénard convection,” *Reviews of Modern Physics* **81**, 503 (2009).
- ²D. Lohse and K.-Q. Xia, “Small-scale properties of turbulent Rayleigh-Bénard convection,” *Annual Review of Fluid Mechanics* **42**, 335–364 (2010).
- ³F. Chillà and J. Schumacher, “New perspectives in turbulent Rayleigh-Bénard convection,” *The European Physical Journal E* **35**, 58 (2012).
- ⁴K.-Q. Xia, “Current trends and future directions in turbulent thermal convection,” *Theoretical and Applied Mechanics Letters* **3**, 052001 (2013).
- ⁵A. Mazzino, “Two-dimensional turbulent convection,” *Physics of Fluids* **29**, 111102 (2017).
- ⁶B.-F. Wang, Q. Zhou, and C. Sun, “Vibration-induced boundary-layer destabilization achieves massive heat-transport enhancement,” *Science Advances* **6**, eaaz8239 (2020).
- ⁷F. Heslot, B. Castaing, and A. Libchaber, “Transitions to turbulence in helium gas,” *Physical Review A* **36**, 5870 (1987).
- ⁸B. Castaing, G. Gunaratne, F. Heslot, L. Kadanoff, A. Libchaber, S. Thomae, X.-Z. Wu, S. Zaleski, and G. Zanetti, “Scaling of hard thermal turbulence in Rayleigh-Bénard convection,” *Journal of Fluid Mechanics* **204**, 1–30 (1989).

- ⁹K.-Q. Xia and S.-L. Lui, “Turbulent thermal convection with an obstructed sidewall,” *Physical Review Letters* **79**, 5006 (1997).
- ¹⁰X.-D. Shang, P. Tong, and K.-Q. Xia, “Scaling of the local convective heat flux in turbulent Rayleigh-Bénard convection,” *Physical Review Letters* **100**, 244503 (2008).
- ¹¹Y.-H. Yang, X. Zhu, B.-F. Wang, Y.-L. Liu, and Q. Zhou, “Experimental investigation of turbulent Rayleigh-Bénard convection of water in a cylindrical cell: The Prandtl number effects for $Pr > 1$,” *Physics of Fluids* **32**, 015101 (2020).
- ¹²R. M. Kerr, “Rayleigh number scaling in numerical convection,” *Journal of Fluid Mechanics* **310**, 139–179 (1996).
- ¹³R. Verzicco and R. Camussi, “Numerical experiments on strongly turbulent thermal convection in a slender cylindrical cell,” *Journal of Fluid Mechanics* **477**, 19–49 (2003).
- ¹⁴B. I. Shraiman and E. D. Siggia, “Heat transport in high-Rayleigh-number convection,” *Physical Review A* **42**, 3650 (1990).
- ¹⁵E. D. Siggia, “High Rayleigh number convection,” *Annual Review of Fluid Mechanics* **26**, 137–168 (1994).
- ¹⁶S. Grossmann and D. Lohse, “Scaling in thermal convection: a unifying theory,” *Journal of Fluid Mechanics* **407**, 27–56 (2000).
- ¹⁷S. Grossmann and D. Lohse, “Fluctuations in turbulent Rayleigh-Bénard convection: the role of plumes,” *Physics of Fluids* **16**, 4462–4472 (2004).
- ¹⁸G. L. Kooij, M. A. Botchev, E. M. Frederix, B. J. Geurts, S. Horn, D. Lohse, E. P. van der Poel, O. Shishkina, R. J. Stevens, and R. Verzicco, “Comparison of computational codes for direct numerical simulations of turbulent Rayleigh-Bénard convection,” *Computers & Fluids* **166**, 1–8 (2018).
- ¹⁹C. Sun, H.-D. Xi, and K.-Q. Xia, “Azimuthal symmetry, flow dynamics, and heat transport in turbulent thermal convection in a cylinder with an aspect ratio of 0.5,” *Physical Review Letters* **95**, 074502 (2005).
- ²⁰H.-D. Xi and K.-Q. Xia, “Flow mode transitions in turbulent thermal convection,” *Physics of Fluids* **20**, 055104 (2008).
- ²¹S. Weiss and G. Ahlers, “Turbulent Rayleigh-Bénard convection in a cylindrical container with aspect ratio $\gamma = 0.50$ and Prandtl number $Pr = 4.38$,” *Journal of Fluid Mechanics* **676**, 5–40 (2011).
- ²²E. P. van der Poel, R. J. Stevens, and D. Lohse, “Connecting flow structures and heat flux in turbulent Rayleigh-Bénard convection,” *Physical Review E* **84**, 045303 (2011).

- ²³E. P. van der Poel, R. J. Stevens, K. Sugiyama, and D. Lohse, “Flow states in two-dimensional Rayleigh-Bénard convection as a function of aspect-ratio and Rayleigh number,” *Physics of Fluids* **24**, 085104 (2012).
- ²⁴H.-D. Xi, Y.-B. Zhang, J.-T. Hao, and K.-Q. Xia, “Higher-order flow modes in turbulent Rayleigh-Bénard convection,” *Journal of Fluid Mechanics* **805**, 31–51 (2016).
- ²⁵F. Pétrélis, S. Fauve, E. Dormy, and J.-P. Valet, “Simple mechanism for reversals of Earth’s magnetic field,” *Physical Review Letters* **102**, 144503 (2009).
- ²⁶B. Gallet, J. Herault, C. Laroche, F. Pétrélis, and S. Fauve, “Reversals of a large-scale field generated over a turbulent background,” *Geophysical & Astrophysical Fluid Dynamics* **106**, 468–492 (2012).
- ²⁷K. Petschel, M. Wilczek, M. Breuer, R. Friedrich, and U. Hansen, “Statistical analysis of global wind dynamics in vigorous Rayleigh-Bénard convection,” *Physical Review E* **84**, 026309 (2011).
- ²⁸M. Chandra and M. K. Verma, “Dynamics and symmetries of flow reversals in turbulent convection,” *Physical Review E* **83**, 067303 (2011).
- ²⁹J. L. Lumley, *The structure of inhomogeneous turbulent flows* (Nauka, 1967).
- ³⁰G. Berkooz, P. Holmes, and J. L. Lumley, “The proper orthogonal decomposition in the analysis of turbulent flows,” *Annual Review of Fluid Mechanics* **25**, 539–575 (1993).
- ³¹S. Chen and G. D. Doolen, “Lattice Boltzmann method for fluid flows,” *Annual Review of Fluid Mechanics* **30**, 329–364 (1998).
- ³²C. K. Aidun and J. R. Clausen, “Lattice-Boltzmann method for complex flows,” *Annual Review of Fluid Mechanics* **42**, 439–472 (2010).
- ³³A. Xu, W. Shyy, and T. Zhao, “Lattice Boltzmann modeling of transport phenomena in fuel cells and flow batteries,” *Acta Mechanica Sinica* **33**, 555–574 (2017).
- ³⁴H. Huang, M. Sukop, and X. Lu, *Multiphase lattice Boltzmann methods: Theory and application* (John Wiley & Sons, 2015).
- ³⁵A. Xu, L. Shi, and T. Zhao, “Accelerated lattice Boltzmann simulation using GPU and OpenACC with data management,” *International Journal of Heat and Mass Transfer* **109**, 577–588 (2017).
- ³⁶A. Xu, L. Shi, and H.-D. Xi, “Lattice Boltzmann simulations of three-dimensional thermal convective flows at high Rayleigh number,” *International Journal of Heat and Mass Transfer* **140**, 359–370 (2019).

- ³⁷A. Xu, L. Shi, and H.-D. Xi, “Statistics of temperature and thermal energy dissipation rate in low-Prandtl number turbulent thermal convection,” *Physics of Fluids* **31**, 125101 (2019).
- ³⁸A. Xu, S. Tao, L. Shi, and H.-D. Xi, “Transport and deposition of dilute microparticles in turbulent thermal convection,” *Physics of Fluids* **32**, 083301 (2020).
- ³⁹A. N. Kolmogorov, “The local structure of turbulence in incompressible viscous fluid for very large Reynolds numbers,” *Doklady Akademii Nauk SSSR* **30**, 301–305 (1941).
- ⁴⁰G. K. Batchelor, “Small-scale variation of convected quantities like temperature in turbulent fluid Part 1. General discussion and the case of small conductivity,” *Journal of Fluid Mechanics* **5**, 113–133 (1959).
- ⁴¹G. Silano, K. Sreenivasan, and R. Verzicco, “Numerical simulations of Rayleigh–Bénard convection for Prandtl numbers between 10^{-1} and 10^4 and rayleigh numbers between 10^5 and 10^9 ,” *Journal of Fluid Mechanics* **662**, 409–446 (2010).
- ⁴²S. Aumaître and S. Fauve, “Statistical properties of the fluctuations of the heat transfer in turbulent convection,” *EPL (Europhysics Letters)* **62**, 822 (2003).
- ⁴³Y. Zhang, Q. Zhou, and C. Sun, “Statistics of kinetic and thermal energy dissipation rates in two-dimensional turbulent Rayleigh–Bénard convection,” *Journal of Fluid Mechanics* **814**, 165–184 (2017).
- ⁴⁴M. Chandra and M. K. Verma, “Flow reversals in turbulent convection via vortex reconnections,” *Physical Review Letters* **110**, 114503 (2013).
- ⁴⁵M. K. Verma, S. C. Ambhire, and A. Pandey, “Flow reversals in turbulent convection with free-slip walls,” *Physics of Fluids* **27**, 047102 (2015).
- ⁴⁶Q. Wang, S.-N. Xia, B.-F. Wang, D.-J. Sun, Q. Zhou, and Z.-H. Wan, “Flow reversals in two-dimensional thermal convection in tilted cells,” *Journal of Fluid Mechanics* **849**, 355–372 (2018).
- ⁴⁷X. Chen, S.-D. Huang, K.-Q. Xia, and H.-D. Xi, “Emergence of substructures inside the large-scale circulation induces transition in flow reversals in turbulent thermal convection,” *Journal of Fluid Mechanics* **877** (2019).
- ⁴⁸S. Wagner and O. Shishkina, “Aspect-ratio dependency of Rayleigh–Bénard convection in box-shaped containers,” *Physics of Fluids* **25**, 085110 (2013).
- ⁴⁹K. L. Chong, S. Wagner, M. Kaczorowski, O. Shishkina, and K.-Q. Xia, “Effect of Prandtl number on heat transport enhancement in Rayleigh–Bénard convection under geometrical confinement,” *Physical Review Fluids* **3**, 013501 (2018).

- ⁵⁰K.-Q. Xia, C. Sun, and S.-Q. Zhou, “Particle image velocimetry measurement of the velocity field in turbulent thermal convection,” *Physical review E* **68**, 066303 (2003).
- ⁵¹B. Podvin and A. Sargent, “A large-scale investigation of wind reversal in a square Rayleigh–Bénard cell,” *Journal of Fluid Mechanics* **766**, 172–201 (2015).
- ⁵²B. Podvin and A. Sargent, “Precursor for wind reversal in a square Rayleigh–Bénard cell,” *Physical Review E* **95**, 013112 (2017).
- ⁵³A. Castillo-Castellanos, A. Sargent, B. Podvin, and M. Rossi, “Cessation and reversals of large-scale structures in square Rayleigh–Bénard cells,” *Journal of Fluid Mechanics* **877**, 922–954 (2019).
- ⁵⁴L. Soucasse, B. Podvin, P. Rivière, and A. Soufiani, “Proper orthogonal decomposition analysis and modelling of large-scale flow reorientations in a cubic Rayleigh–Bénard cell,” *Journal of Fluid Mechanics* **881**, 23–50 (2019).
- ⁵⁵J. N. Kutz, S. L. Brunton, B. W. Brunton, and J. L. Proctor, *Dynamic mode decomposition: data-driven modeling of complex systems* (SIAM, 2016).
- ⁵⁶S. L. Brunton and J. N. Kutz, *Data-driven science and engineering: Machine learning, dynamical systems, and control* (Cambridge University Press, 2019).